An Investigation on Microstructure and Mechanical Properties of Nd:YAG Laser Beam Weld of Copper Beryllium Alloy

S.A.A. AKBARI MOUSAVI and S.T. NIKNEJAD

Nd:YAG pulsed laser beam welding is conducted on UNS-C17200 copper beryllium sheet. Welding is carried out in the as-annealed and as-aged conditions to investigate the effects of preweld condition on weld microstructure and mechanical properties. Two different heat treatments including direct age treating and solution annealing + subsequent age treating are considered after welding. The mechanical and microstructural characteristics of weld metal regions (WMs) and heat-affected zones (HAZ) of four different samples are considered using tensile tests, hardness measurements, optical microscopy, electron microscopy, and X-ray diffraction (XRD). Results indicate that the microstructural and mechanical properties of the HAZ without postweld treatment are adversely affected by grain boundary liquation observed if welding is carried out in the as-aged condition. Tensile strength and hardness of the WM are improved after a postweld artificial age treatment at 315 °C for 3 hours. However, hardness of the WM is lower than that of the base metal (BM) and HAZ, because the precipitation mechanism in the fusion zone is not as effective as that is in the HAZ and BM. The CuBe secondary phase precipitates during solidification. The precipitates/matrix interface is incoherent, which does not significantly raise the hardness of the weld metal. Incoherent interdendritic precipitates are dissolved in the weld structure after postweld solution annealing. Having performed postweld solution treatment and aging, full strength and hardness throughout the copper beryllium material were observed.

DOI: 10.1007/s11661-009-9822-4
© The Minerals, Metals & Materials Society and ASM International 2009

I. INTRODUCTION

PRECIPITATED-HARDENING copper beryllium alloy is widely used in various kinds of springs due to its low elastic module and high strength. This alloy is solution annealed to raise its formability and precipitation hardened (age hardened) to increase its strength. Figure 1 shows the binary diagram of Cu-Be and the behavior of C17200 alloy. The microstructure consists of α phase in the 650 °C to 900 °C temperature range. By quenching from this temperature range, the supersaturated α is produced. If the aging treatment for the copper beryllium alloy is carried out below the 550 °C, the CuBe intermetallic phase would precipitate at the grain boundaries in the forms of GP zone, γ'', γ', and γ.[1]

Few investigations have been carried out on the precipitation behavior of copper and copper alloys.[2–5] Their finding suggested the following precipitation *sequences* for the Cu-Be alloy: supersaturated $\alpha \rightarrow$ GP zone $\rightarrow$ coherent $\gamma'' \rightarrow$ semicoherent $\gamma' \rightarrow$ incoherent γ. Era and Kishitake[4] studied the microstructure of age-treated alloy by transmission electron microscopy (TEM) bright field. Their TEM images revealed the striations emerged within the α grains due to contraction of lattice parameter.

The C17200 alloy exhibits two different behaviors during solidification. In the equilibrium conditions, the α phase nucleates and the alloy keeps its single-phase condition below the solidus line. If the solidification is carried out in the nonequilibrium condition, which is usual in any low energy fusion welding processes, it is more likely that β phase is formed by peritectic reaction. The β phase does not reserve its stability at room temperature and decomposes to α and γ.

Few investigations have been carried out on the microstructure and properties of copper and copper alloys weldment. Zalkind *et al.*[6] studied the effect of postweld age treatment on the electron beam weld of the C17200 alloy. They found no sharp increase on the hardness of weld metal after the age treatment due to precipitation of incoherent γ phase. On the contrary, they showed that hardness of the heat-affected zone was raised significantly after aging heat treatments. The authors attributed the reasons to the severe thermal cycles formed during the welding and subsequent solution annealing occurring in the HAZ. Nd:YAg pulsed laser welding is known as an appropriate process for joining materials with the high thermal conductivity coefficient. Nd:YAG pulsed laser welding also enables welding of plates with little nominal thickness due to low heat input introduced in joint sections. In this research, butt welding of copper beryllium plate was carried out with the nominal thickness of 0.2 mm in order to manufacturing a workpiece with resilient properties.

S.A.A. AKBARI MOUSAVI, Associate Professor, and S.T. NIKNEJAD, Research Assistant, are with the School of Metallurgy and Materials Engineering, University College of Engineering, University of Tehran, Tehran 14395-515, Iran. Contact e-mail: akbarimusavi@ut.ac.ir

Manuscript submitted October 18, 2008.
Article published online April 21, 2009

II. EXPERIMENTAL PROCEDURE

The UNS-C17200 (Cu-1.9 wt pct Be-0.4 wt pct Co) plate was used in this investigation with the nominal thickness of 0.2 mm. The Nd:YAG-pulsed laser welding was carried out with an SW-1 microlaser machine. The maximum average power of laser used was 80 W. Welding procedures were carried out in 30 seconds for each sample with the optimum laser parameters (Table I),

The various types of heat treatment carried out before and after welding are as follows:

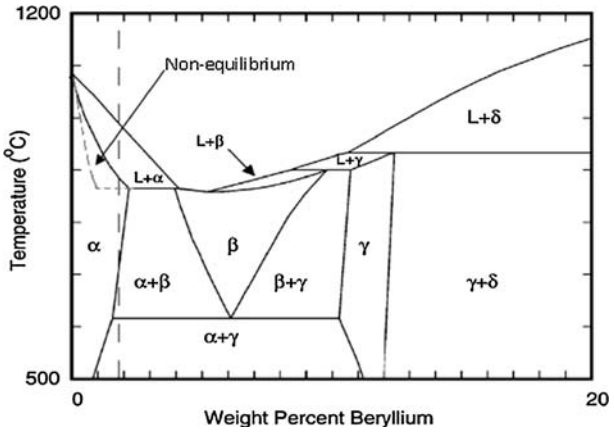

Fig. 1—Cu-Be diagram in equilbrium and nonequilbrium conditions.[3]

(1) solution annealing treatment at 790 °C for 15 minutes, and
(2) artificial age hardening treatment at 315 °C for 360 minutes.

The sequence of heat treatment for each sample is shown in Table II. The samples were thereafter cut in cross section. The etching process was performed by immersion of the samples in ammonium persulfate-hydroxide solution (2 parts 10 pct NH_4OH, 1 part 3 pct H_2O_2, and 6 parts H_2O). In this study, the micrographs of the weld pool and heat affected zone (HAZ) of the samples that have undergone various pre- and postheat treatments are compared by optical microscopy and scanning electron microscopy (SEM). Micro-Vickers hardness measurements are conducted on the etched cross section of the welds with a load of 0.2 Kgf holding for 15 seconds. Tensile tests are carried out according to ASTM-E8 at a strain rate of 3.28×10^{-4} s^{-1} and the results are tabulated in Table III. The shape and dimensions of the tensile samples are, according to the subsize specimen, presented in Figure 2.

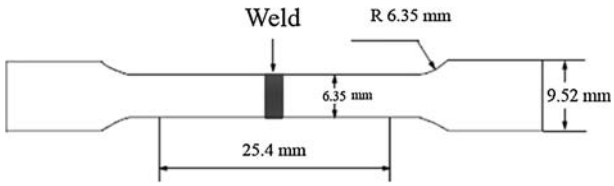

Fig. 2—Schematic diagram of tensile specimen.

Table I. Parameters for Laser Welding of Copper Beryllium Material

Laser Welding Parameter	Pulse Voltage (V)	Pulse Duration (ms)	Focused Beam Diameter (mm)	Pulse Frequency (Hz)	Welding Speed (cm/min)
	460	4	0.2	10	12

Table II. Sequence of Welding and Heat Treating Procedures for Samples

Sample Name	Procedure			
SW	solution annealing	welding	—	—
AW	solution annealing	age treating	welding	—
SWA	solution annealing	welding	age treating	—
SWSA	solution annealing	welding	solution annealing	age treating

Table III. Tensile Properties and Location of Fracture in Welded Samples

Property	Annealed	SW	AW	SWA	SWSA (No Final Age Treatment)	SWSA
Yield stress (MPa)	754	516	567	888	642	902
Tensile strength (MPa)	799	737	742	1108	755	1372
Elongation (Pct)	11.04	2.01	1.4	0.96	9.59	3.18
Mode of fracture	ductile	ductile-brittle	ductile-brittle	brittle-ductile	ductile	ductile
Fracture location	—	HAZ	HAZ	weld	base	base

III. RESULTS

A. *Base Metal Structure*

The SEM micrograph and X-ray diffraction (XRD) pattern of annealed copper beryllium alloy are shown in Figures 3(a) and (b), respectively. The annealed microstructure mainly consists of α grains in which the beryllium atoms are dissolved. The white particles dispersed throughout the structure are intermetallic cobalt-beryllide phase.[1] The particles have high melting point (~1090 °C)[7] and, thus, reserve their stability during extreme thermal cycles (Figure 3(a)). For the aged microstructure (Figure 4(a)), grain boundaries are thicker and rougher than those observed in the annealed structure (Figure 3(a)). Grain boundary coarsening is due to γ'', γ', and γ precipitation during the artificial age treatment.[1] Precipitation could also be detected by XRD analysis (Figure 4(c)). The interface of precipitate/matrix is mostly coherent or semicoherent. Moreover, the lattice parameter of the precipitates is much lower than that of the α phase, which results in lattice strains in the microstructure. Consequently, striations appear within the grains due to the contraction in the α-matrix grains, resulting in a rather rough grain structure (Figure 4(b)). Era and Kishitake claimed that the striations are mostly parallel to the (011) planes of the α matrix.[4]

B. *Weld Metal and HAZ*

The weld metal zone microstructure of the SW sample is shown in Figure 5. Three different morphologies of the solidified structure are distinctive in the weld pool. A columnar structure is formed adjacent to the fusion boundary. The direction of these columns is parallel to the thermal gradient in the weld pool (*i.e.*, toward the weld centerline) and in an easy-growth solidification direction of lattice structure. Secondary dendrite arms form at the columnar structure. Advancing toward the weld centerline, the secondary dendrite arms as well as the columnar structure disappear and are replaced by equiaxed dendrites. As a result, a fully equiaxed structure is the dominant morphology adjacent to the weld centerline. The thermal gradient (G) decreases from the fusion boundary to the weld centerline, while the solidification rate (R) increases. The reason can be described by Eq. [1]:[8]

$$R = v \cdot \cos\alpha \qquad [1]$$

where v is the welding speed and α is the angle between the welding direction and normal to fusion boundary. Consequently, there is a decline in the ratio of G:R from the fusion boundary toward the weld centerline, which is associated with the amount of the undercooling in the weld metal. In other words, the undercooling reaches its minimum magnitude near the weld centerline, which is the reason for the equiaxed dendrite formation.

As shown in Figures 3(b) and 4(c), the maximum peak intensity of the XRD patterns for the base metal (BM) is obtained for (220) crystallographic planes. However, the maximum peak achieved in the weld metal is along the (200) crystallographic planes (Figure 6). This difference indicates that the easy-growth crystallographic planes for the solidification of copper alloys are {200}. The results are in accordance with other research.[9,10] Moreover, the easy-growth solidification direction is perpendicular to the {200} planes, *i.e.*, [100], the preferred solidification direction in the fcc materials.[11] The XRD graph also implies that γ-CuBe phase forms during the solidification of the weld metal. Having compared Figure 4(c) with Figure 6, it can be concluded that the precipitation of γ-CuBe is incomplete during the cooling of the weld metal.

The microstructures of the heat-affected zones of SW (welding was carried out in as-aged condition) and AW (welding was carried out in as-aged condition) samples are shown in Figures 7(a) and (b) respectively. The irregular and jagged shapes of the grain boundaries

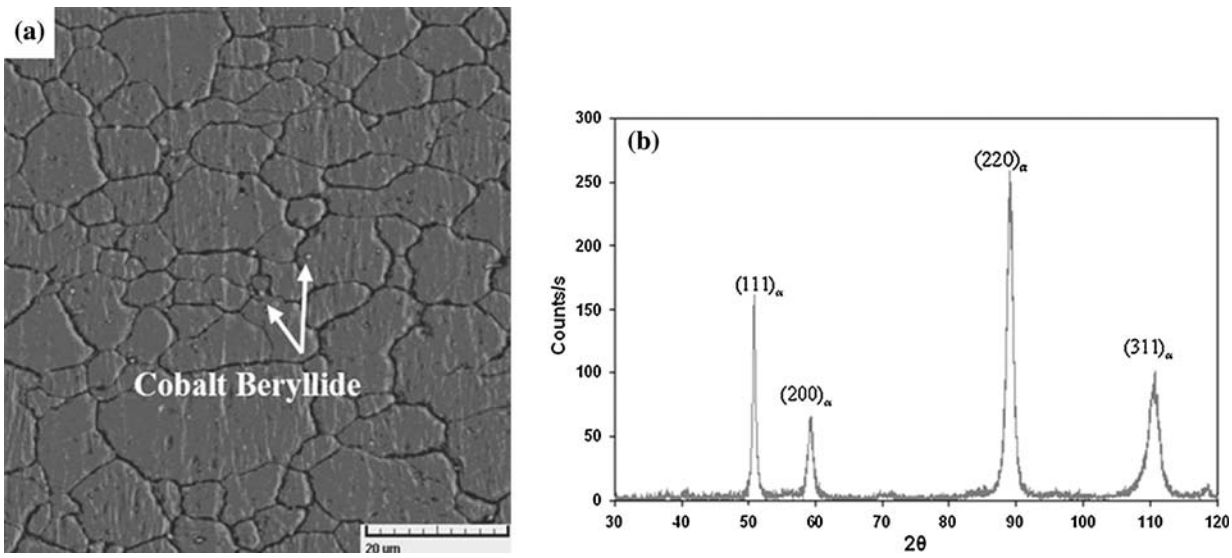

Fig. 3—(*a*) Microstructure and (*b*) XRD pattern of as-annealed parent metal, UNS-C17200.

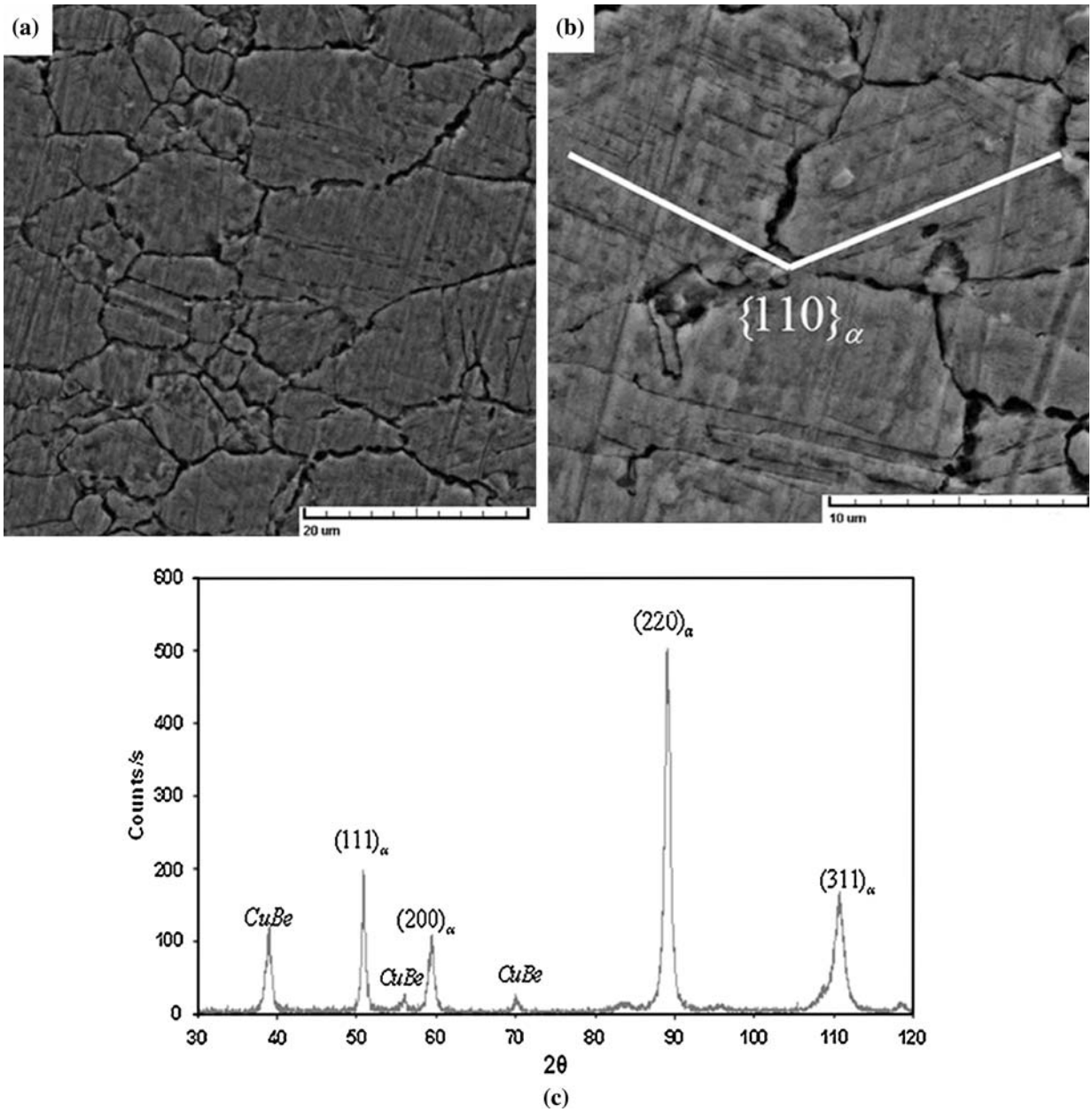

Fig. 4—(*a*) and (*b*) Microstructure and (*c*) XRD pattern of as artificial aged parent metal, UNS-C17200.

adjacent to the fusion boundaries are the characteristic features of grain boundary liquation.[12] During the age treatment, precipitation occurs at grain boundaries so that the accumulation of beryllium atoms drops the melting point of the matrix/precipitate. Hence, if welding is carried out after the age treatment, during the heavy thermal cycles of welding, constitutional liquation occurs, which weakens the grain boundaries. Grain boundary liquation of the HAZ in the SW sample is probably due to the diffusion of beryllium atoms toward grain boundaries during welding, which lowers the melting point. Following the existence of the heavy transient stress field induced during welding, the probability of grain boundary cracking increases. Tensile stresses increase substantially when the welding is carried out in the as-aged condition, and consequently liquation cracking becomes very probable (Figure 7(b)). The hardness of the copper beryllium structure is enhanced substantially after age treatment. Consequently, transient thermal stresses induced during the welding process are raised in the AW sample. The heavy transient stress field is accompanied by grain boundary weakening and causes grain boundary cracking in the AW sample (Figure 7(b)). The XRD pattern of the HAZ in the SW sample in illustrated in Figure 7(c). Contrary to the weld metal, the secondary phase is not formed in the HAZ.

Figure 8 shows the hardness profiles of both SW and AW samples. As can be seen from the hardness profile of the SW sample, the hardness of the weld pool is relatively higher than that of the HAZ and BM. According to the XRD results shown in Figure 6, the

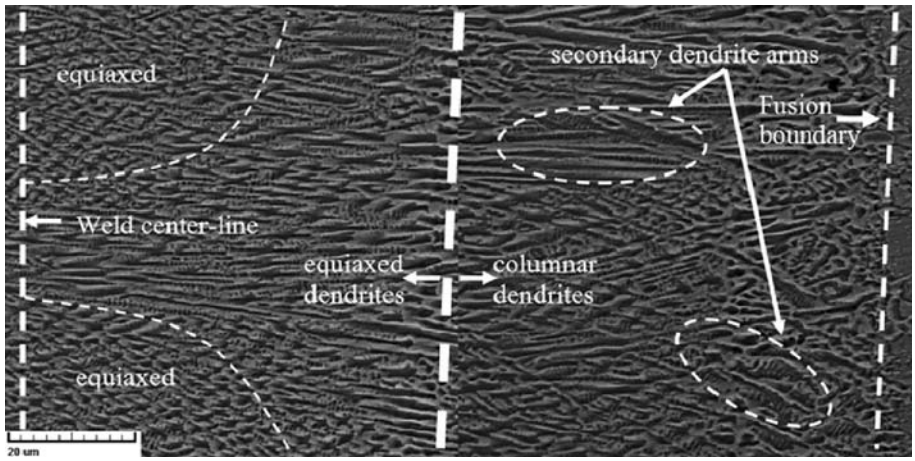

Fig. 5—Microstructure of weld fusion zone–SW sample.

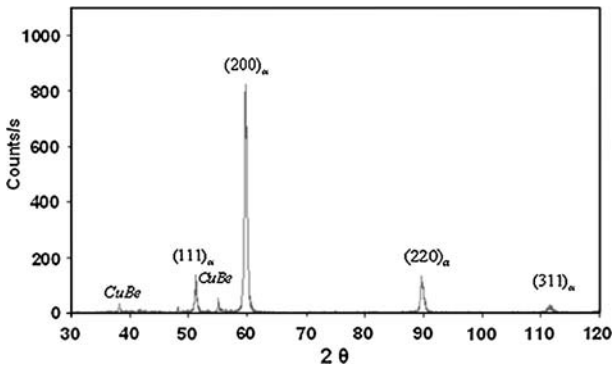

Fig. 6—XRD pattern of weld metal–SW sample.

weld metal structure consists of α and intermetallic CuBe phases. Moreover, the XRD pattern of the HAZ shows no signs of secondary phase formation after welding (Figure 7(c)). Consequently, it is suggested that the CuBe secondary phase is responsible for the small increase in the weld metal hardness. More precise observation shows that the weld metal near the center-line is slightly harder than the region adjacent to the HAZ. This is probably due to a grain refinement after overlapping of the welding pulses, which occurs in the internal section of the fusion zone. In other words, the dendritic structure of the first pulse is broken down by the subsequent pulse in the pulse overlapping region, and thus, finer dendrites form after resolidification. For the AW sample, there is another scenario. The hardness values of the weld metal and HAZ are extremely lower than those of the BM. It can be inferred that the thermal cycles of the welding process have caused the complete dissolution of secondary CuBe phase in the HAZ structure in the AW sample.

C. *Postweld Heat Treatment*

The microstructure of the HAZ after the postweld age treatment is shown in Figure 9(a) (sample SWA in Table II). Adjacent to the fusion boundary, the grain boundary liquation has mostly disappeared. However, a few slight signs of liquation are still observed. The aging has no major effects on the weld pool microstructure, because it is carried out at temperatures far below the solution temperature. Striations are evident in the HAZ, which is an implication of the precipitation forming during the postweld age treatment.

Figures 9(b) through (d) show the weld metal and HAZ microstructures after the postweld solution annealing and subsequent aging treatment (sample SWSA in Table II). As is obvious, in the weld metal region (WM), the solidified structure has disappeared. Oriented grains have replaced the columnar structure, and coarse equiaxed grains have taken the place of the dendrites. Each grain is formed from a cluster of the solidified cells or dendrites, which have the same orientation.[13] Figures 9(b) and (c) also show that the liquation cracking is completely removed in the HAZ. Striations are observed within the grains of the weld microstructure, which implies a successful aging process (Figure 9(d)). Figure 9(e) shows an XRD graph of weld metal in the SWSA sample. As compared to Figure 6, the relative intensities of the CuBe phase in the weld metal have been raised after solution annealing and subsequent aging, which implies the complete precipitation after postweld heat treatment.

Figure 10 compares the microhardness profile across the weld pool before and after the postweld heat treatments. The figure shows that the weld metal hardness of the SWA sample is higher than that of the SW sample, but lower than that of its BM. The hardness first increases to 340 HV in the HAZ adjacent to the weld metal, and then returns to the hardness of the BM (360 HV) after a short decline. After the postweld solution annealing and subsequent aging (for SWSA sample), however, a consistent hardness trend is obtained across the weld pool. As can be seen, full hardness is obtained throughout the WM and the HAZ.

Mechanical properties and fracture modes of the specimens are presented in Table III. As can be seen, the welding processes without the postweld treatments weaken such mechanical properties as tensile strength

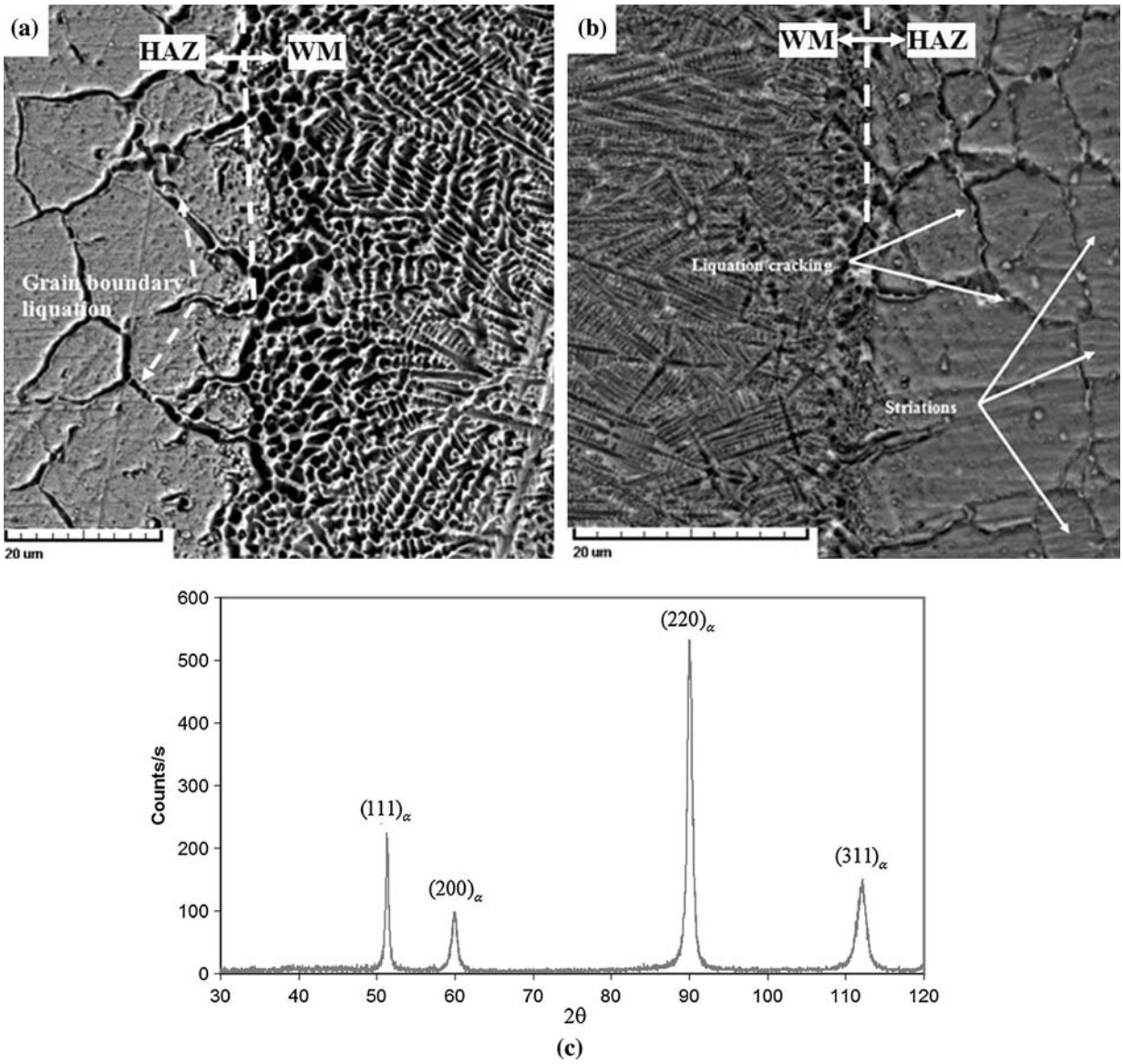

Fig. 7—Microstructure of heat affected zone: (*a*) SW sample, (*b*) AW sample, and (*c*) XRD pattern of HAZ-SW sample.

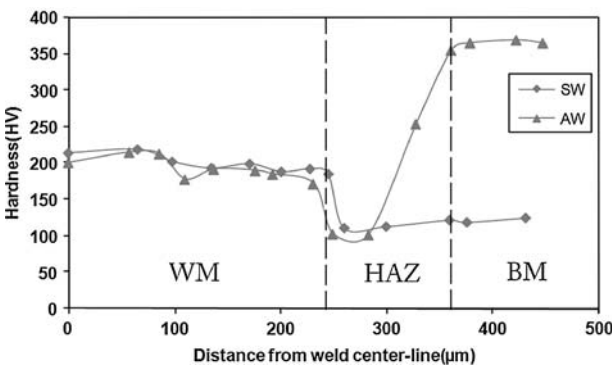

Fig. 8—Micro-Vickers hardness profile of SW and AW samples.

and elongation. By the postweld age treatment, the tensile strength of a weld sample increases (for SWA sample), whereas the elongation decreases. The mechanical properties of a weld sample are enhanced after the postweld solution annealing and subsequent aging (for SWSA sample).

Figure 11 shows the SEM images of the fracture surface micrographs of annealed, SW, SWA, and SWSA (before and after age treatment) samples, respectively. The annealed sample shows 100 pct ductile fracture throughout the fracture surface (Figure 11(a)). Microvoid coalescence is obvious in the top right magnified image. The fracture of the SW sample converts to a ductile-brittle mode (Figure 11(b)); microvoid coalescence can be observed in the middle part of the fractured surface. The fracture mode of the AW sample is almost the same as the SW sample (Figure 11(c)). Having compared image (b) with (d), it can be observed that the postweld age treatment has stimulated a brittle fracture in the SWA sample (Figure 11(d)). In addition, in the latter image, a cleavage fracture can also be detected by the "river marking." In the SWSA sample (either before

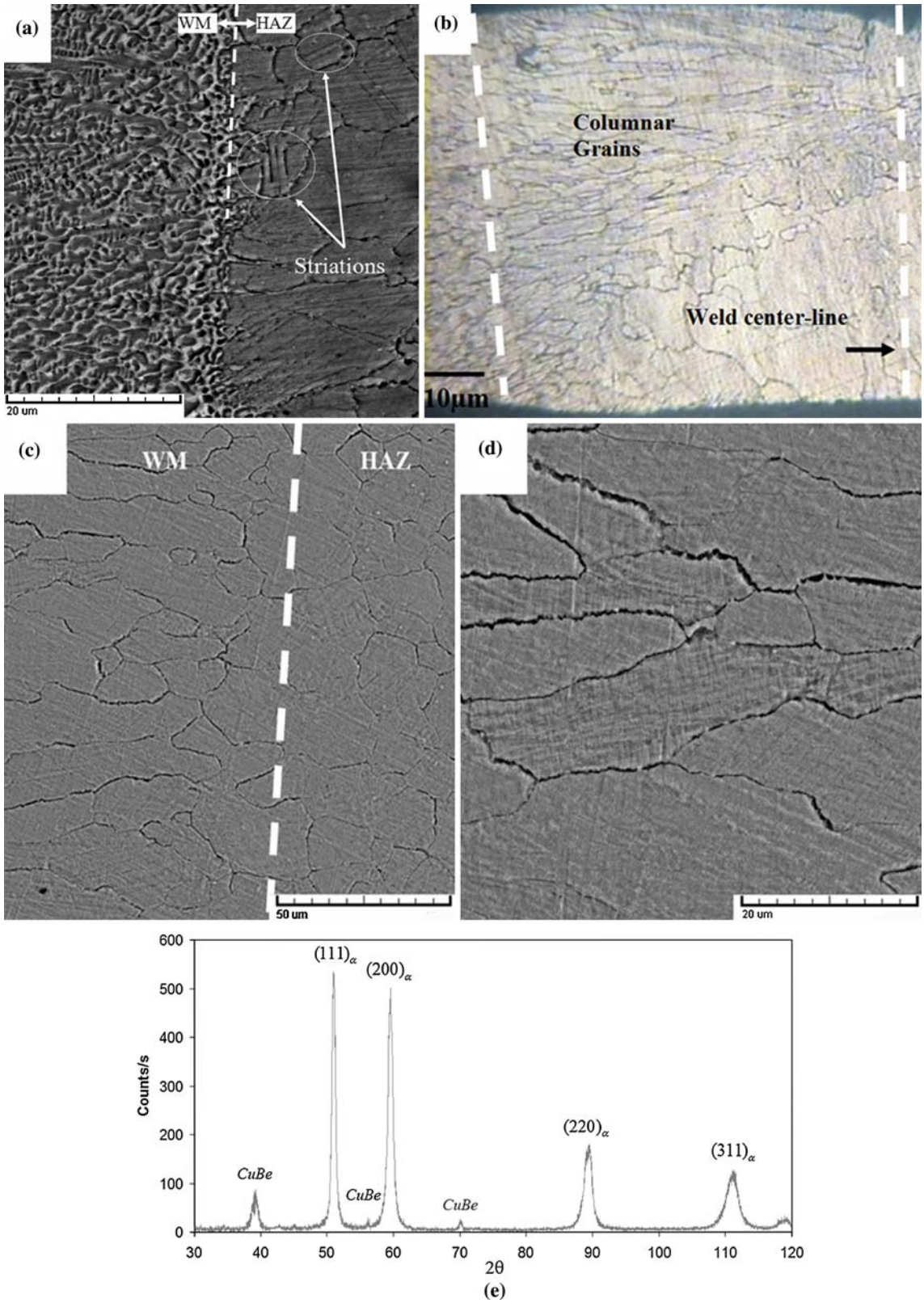

Fig. 9—Microstructure of weld and HAZ for (*a*) an SWA sample and (*b*) and (*c*) an SWSA sample. (*d*) Striations within the weld metal grain and (*e*) XRD pattern of the weld metal–SWSA sample.

or after age treatment), fracture is 100 pct ductile, and the existence of the shallow voids (Figures 11(e) and (f)) is the characteristic of a transgranular fracture.[14] Figure 11(f) shows that the microvoids in the fracture surface of the SWSA sample are smaller than those obtained in the annealed sample and the SWSA sample

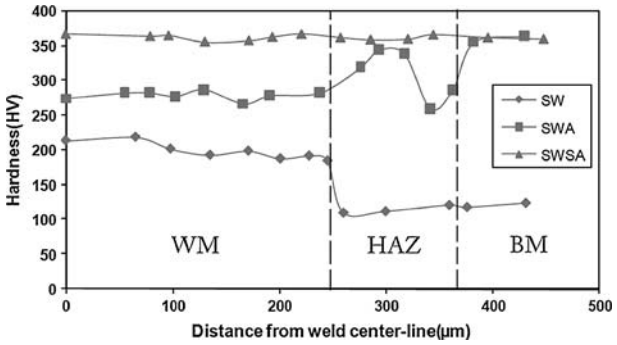

Fig. 10—Micro-Vickers hardness profile of SWA and SWSA samples.

before age treatment (Figures 11(a) and (e)), which could have led to a substantial increase in the tensile strength of the SWSA sample (Table III).

IV. DISCUSSION

At the initial stages of solidification, the α phase nucleates and grows in the form of cells and dendrites (gray-colored structures in Figure 5), which enriches the solute content of interdendritic residual liquid (black-colored structures in Figure 5). Consequently, the peritectic reaction ($L + \alpha \rightarrow \beta$) occurs at interdendritic regions according to the Cu-Be equilibrium phase diagram (Figure 1). The compositional difference explains why the interdendritic regions are more affected during the etching treatment in comparison with the dendrite cores. Because they have more energy, the interdendritic regions corrode more than the dendritic cores do during the etching treatment. The β phase is not stable at temperatures below 650 °C and, thus, transforms into α and γ. According to the XRD patterns (Figures 6 and 9(e)), the relative peak intensities of the CuBe phase in the weld metal of the SW sample are not as high as the ones in the SWSA sample. This observation suggests that the precipitation during welding is a nonequilibrium process, which results in incomplete formation of the secondary phase. Moreover, the interface of the precipitate/matrix is incoherent; thus, the hardness of the weld metal is not substantially effected (Figure 8).

From the hardness measurements (Figure 8) and fracture location (Table III) associated with SW and AW samples, it can be concluded that HAZ is the weakest region throughout the microstructure of these samples. Two mechanisms may describe the hardness reduction in the HAZ. First, liquation cracking, as shown in Figure 7, occurs during the welding in the HAZ. Liquation cracking has an adverse effect on grain boundary strength. Second, most of the γ' and γ'' precipitates are dissolved in the α matrix due to the severe thermal cycle that exists in the HAZ during welding. This phenomenon is called "reversion of precipitates," which occurs when the HAZ is heated to the precipitation temperature range and causes the dissolution of secondary CuBe phase in the structure. Reversion of the second phase ranges from partial reversion at the HAZ/unaffected zone interface to full reversion near the fusion boundary.

In the HAZ, adjacent to the weld metal, the temperature is high enough for full solution treatment. Therefore, complete coherent and semicoherent precipitation is achieved during the postweld age treatment, which results in the maximum hardness value in the HAZ of the SWA sample (Figure 10). The hardness measurements of the HAZ are in conformity with Zalkind's research.[6]

As mentioned previously, incomplete precipitation occurs in the weld metal, leaving the structure partially saturated by solute content. Thus, precipitation in the weld metal is not as effective as that is in the HAZ during the postweld age treatment. Moreover, the age treatment coarsened the incoherent interdendritic precipitates in the SWA sample. Coarse precipitates obstruct the dislocation movements during the tensile test, which causes dislocation pileup. Dislocation pileup produces microcracks. As can be seen in Figure 11(c), the microcrack coalescence resulted in the brittle fracture, which left behind "river marking" in the surface of the fracture occurring in the WM of the SWA sample.

Annealing at 790 °C is the driving force for diffusion of atoms between dendrites and interdendritic regions and consequent homogenizing. Thus, after postweld annealing, the interdendritic region disappears and the entire weld metal structure is etched uniformly (Figures 9(b) through (d)). Postweld annealing causes the incoherent interdendritic γ to dissolve in the microstructure. The fully supersaturated structure is obtained after quenching the sample. Moreover, this process modifies the grain boundary liquation in the HAZ. This can be realized by the shift of fracture location from HAZ to BM in the SWSA sample without the final age treatment (Table III). Aging treatment after annealing leads to full hardening of material in the weld metal, HAZ, and BM structures (SWSA sample).

V. CONCLUSIONS

A comprehensive investigation of microstructure and mechanical properties of Nd:YAG laser-welded copper beryllium material was carried out in this research. The morphology of weld metal structure varies from columnar structure adjacent to fusion boundary to equiaxed dendrites near the weld centerline. The microstructure of the HAZ is deteriorated by grain boundary liquation after the welding process. Grain boundary liquation is not stable and can be modified by appropriate postweld heat treatment. Postweld age treatment causes the coarsening of incoherent interdendritic precipitates and the brittle mode of fracture in tensile test. These incoherent interdendritic precipitates are dissolved during postweld annealing. Consequently, full hardness and desired mechanical properties are achieved after subsequent full annealing and aging treatment after welding.

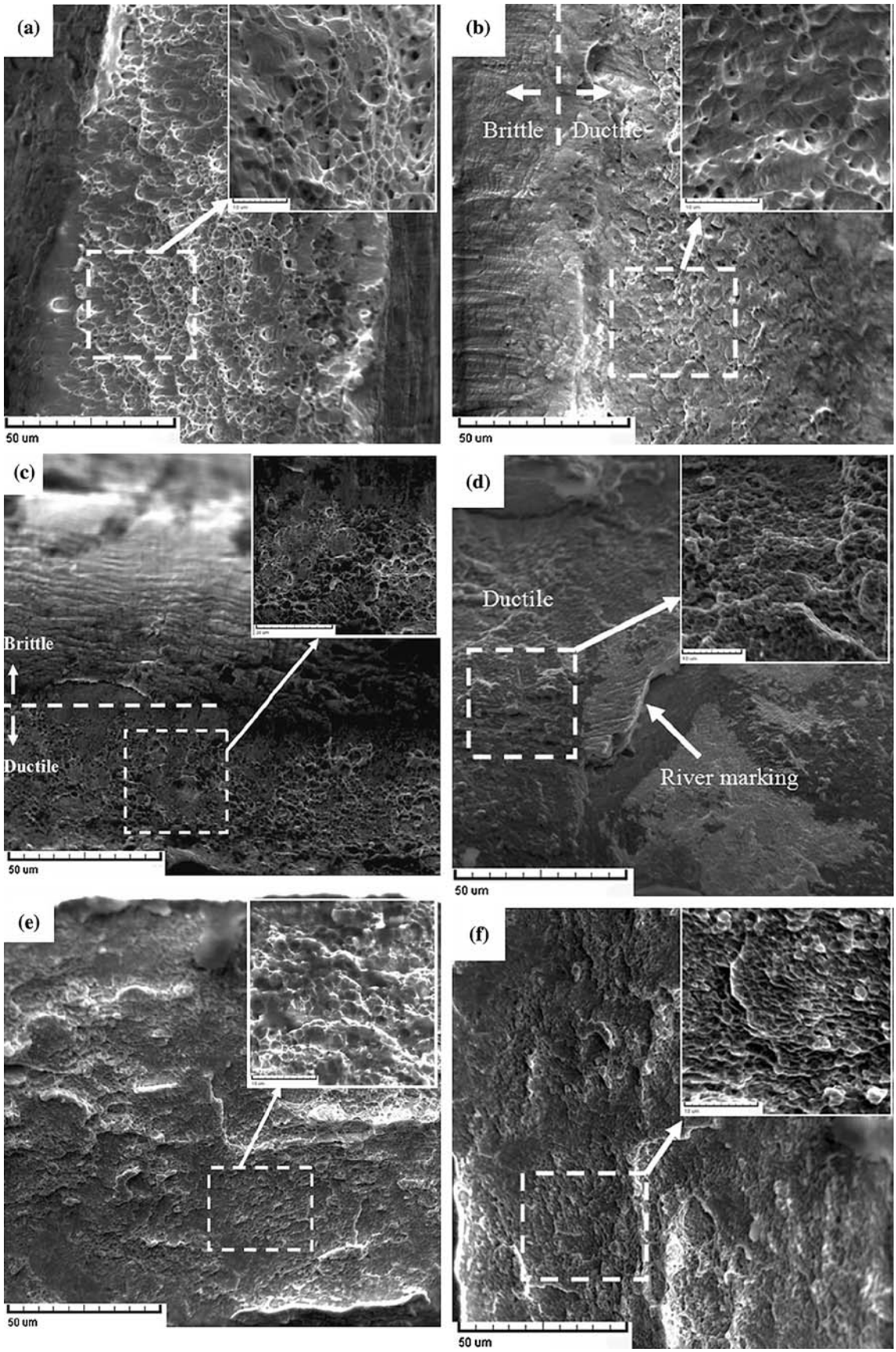

Fig. 11—SEM micrographs of fracture surface: (*a*) annealed sample, (*b*) SW sample, (*c*) AW sample, (*d*) SWA sample, (*e*) SWSA sample without final age treatment, and (*f*) SWSA sample after age treatment.

ACKNOWLEDGMENT

The authors express their gratitude to the School of Metallurgy and Materials Engineering, University of Tehran, for providing SEM and XRD equipments.

REFERENCES

1. J.C. Harkness and A. Guha: *Metallography and Microstructures*, vol. 9, *ASM Handbook*, ASM INTERNATIONAL, Metals Park, OH, 2004, pp. 752–61.
2. R.J. Rioja and D.E. Laughlin: *Metall. Mater. Trans. A*, 1984, vol. 15A, pp. 939–41.
3. W.C. Crone: *J. Cryst. Growth*, 1999, vol. 218, pp. 381–89.
4. H. Era and K. Kishitake: *Metall. Mater. Trans. A*, 2000, vol. 31A, pp. 2765–71.
5. R. Monzen, C. Watanabe, and D. Mino: *Acta Mater.*, 2004, vol. 53 (4), pp. 1153–61.
6. S. Zalkind and D. Moreno: *J. Mater. Sci. Lett.*, 1999, vol. 18, pp. 849–52.
7. *Alloys Phase Diagrams*, vol. 3, *ASM Handbook*, ASM INTERNATIONAL, Metals Park, OH, 2004.
8. S. Kou: *Welding Metallurgy*, Wiley, New York, NY, 2003, p. 155.
9. Z. Zhao, C. Wang, and N. Li: *Appl. Surf. Sci.*, 2006, vol. 252 (11), pp. 4257–63.
10. G.G. Roy, J.W. Elmer, and T. DebRoy: *J. Appl. Phys.*, 2001, vol. 100, pp. 805–903.
11. B. Chalmers: *Principles of Solidification*, Wiley, New York, NY, 1964, p. 117.
12. O.A. Ojo and N.L. Richards: *Scripta Mater.*, 2004, vol. 54, pp. 641–46.
13. C.M. Cheng and C.P. Chou: *Mater. Sci. Technol.*, 2006, vol. 22, pp. 685–90.
14. Y. Rosenthal: *J. Mater. Sci.*, 1992, vol. 27 (8), pp. 2193–98.